Evaluation of a simplified approach for simulating gravity currents over slopes of varying angles

Francois Blanchette [*,a] , Vincent Piche [b] & Eckart Meiburg [a]

[a] *Department of Mechanical Engineering, University of California Santa Barbara, Engineering II, 2355, Santa Barbara, CA 93106, USA*

[b] *École Polytechnique, Paris, France*

Abstract

Using high resolution numerical simulations of the two-dimensional Navier-Stokes equations, we evaluate a conceptually simple approach to modeling gravity currents traveling over a bottom boundary of varying slope. We consider a rectangular computational domain, which allows for simple and efficient implementation of the equations and boundary conditions. Rather than implementing a complete coordinate transformation, the varying slope is modeled through the introduction of a spatially varying gravity vector. Our methodology is validated through studies of mass and energy conservation. The propagation velocity of the current and qualitative features of the flow are also found to be consistent with experimental observations of gravity currents traveling down constant or varying slopes.

Key words: gravity currents, highly resolved simulations, turbidites
PACS: ¿123?, ¿456?, ¿789?

1 Introduction

Gravity currents are formed when a mass of relatively heavy fluid intrudes laterally into a lighter ambient fluid. Density–driven currents are due to compositional, salinity or temperature variations and find applications in rivers flowing into the sea, lava flows and storms in the atmosphere (see Simpson [1]). Suspended particles may also be responsible for the density difference

* Corresponding author
Email address: blanchef@engr.ucsb.edu (Francois Blanchette).
URL: www.me.ucsb.edu/~blanchef (Francois Blanchette).

between heavy and ambient fluid, giving rise to so–called particle–driven currents or turbidites. The particles then settle relative to the fluid and deposit at the bottom surface. Such currents arise mostly in geophysical contexts. For example, the maximal distance traveled by air masses laden with volcanic ash constitutes a great security concern [2]. Also, the deposits left by underwater turbidites may indicate the presence of oil and gas fields ([3], [4]). Recent studies of particle clouds have furthermore underlined the importance of particle–laden gravity currents in the context of the dumping of waste into rivers and oceans [5].

Numerical simulations of particle–laden gravity currents have been performed using the shallow–water equations by, among others, García [6] and Bonnecaze, Huppert & Lister [7]. Such simulations consider layer-averaged quantities and rely on a number of empirical relations to estimate the effects of pressure, turbulence and bottom friction. More recently, direct numerical simulations of two and three–dimensional density and particle–driven gravity currents have been performed by Härtel, Meiburg & Necker [8] and Necker *et al.* [9], thus eliminating the need for such empirical coefficients. However, these simulations are still limited to relatively low Reynolds number ($O(1,000)$) and simple geometries.

Several experimental studies of density or particle gravity currents have been performed in the last 40 years. In particular, Britter & Linden [10] studied the progression of a constant flux of heavy fluid traveling down a constant slope and Beghin, Hopfinger & Britter [11] investigated the evolution of finite volume releases in the same context. Both sets of authors noted that larger slope angles caused increased mixing between light and heavy fluid and slightly faster propagation of the current's front. They also observed that the head of the current was slighty raised above the bottom surface when traveling over an inclined plane. Finite volume releases of particle-laden currents were studied in a shallow ambient by Bonnecaze, Huppert & Lister [7] who noted, among other things, that a bore could form from the reflection of the light fluid backflow. This bore was seen to overtake the head of the current and to alter significantly the dynamics of the flow. Experiments on particle-laden currents flowing down slopes of varying angles were conducted by García & Parker [12] and García [13]; these authors used a constant inflow of particle–laden fluid and focused mostly on the particle deposition patterns.

Many physical applications of gravity currents involve irregular bottom boundaries. Turbidites often travel down continental shelves with varying slopes [14]. Bores may form as gravity currents run over sizable obstacles [15]. Also, in order to provide an accurate description of deposits left by repeated gravity currents, the geometry of earlier deposits must be taken into account in simulations of latter currents [16]. Such currents may be eroding or depositing, depending on the geometry of the boundary, and may be responsible for cer-

tain geological structures such as the formation of underwater canyons and levees [14].

Our objective is to develop a conceptually simple approach which allows to simulate complex geometries, but still uses fast, highly accurate numerical methods. We focus here on two–dimensional simulations of the Navier-Stokes equations applied to gravity currents propagating over a lower boundary of varying slope angle. In most applications, the bottom geometry is slowly varying. We here use the fact that the curvature of the topography is usually small to develop simulations that are simpler and faster than full mappings of the Navier-Stokes equations and which do not require structured meshes or grid generation. We first review the governing equations of motion in §2. We then introduce the numerical model used to simulate the flow in §3 before discussing the validity of our simulations in §4. Our conclusions are presented in §5.

2 Governing Equations

We consider situations where the density difference between heavy and light fluid is relatively small ($< 5\%$). We may therefore use the Boussinesq approximation and consider density variations in the buoyancy term only. We assume that the density of the fluid is linearly related to the concentration, $\bar{C}$, of either a solute or suspended particles, $\bar{\rho} = \bar{\rho}_0(1 + \alpha\bar{C})$, where α is constant and the bars denote dimensional quantities. When simulating turbidites, we consider small Reynolds number particles with settling speed $\bar{U}_s$. We denote by $\bar{h}$ the initial heavy fluid height and by $\bar{C}_0$ the initial solute or particle concentration. We restrict our study to high Reynolds number flows, $Re = \bar{u}_b\bar{h}/\bar{\nu} \sim O(1,000)$, where $\bar{u}_b$ and $\bar{\nu}$ are a characteristic velocity and viscosity of the current. Buoyancy forces are therefore balanced by inertial forces and a typical value of $\bar{u}_b$ is

$$\bar{u}_b = \sqrt{\bar{g}\alpha\bar{C}_0\bar{h}}$$

where $\bar{g}$ is the gravitational acceleration.

In order to keep the computational time manageable, we consider two–dimensional gravity currents. The velocities parallel and perpendicular to the bottom surface are denoted by u_1 and u_2, respectively, and the corresponding coordinates by x_1 and x_2. We introduce a streamfunction ψ such that $u_1 = \partial_{x_2}\psi$ and $u_2 = -\partial_{x_1}\psi$ and a vorticity field $\omega = \partial_{x_1}u_2 - \partial_{x_2}u_1$. The angle between the bottom surface, $x_2 = 0$, and the horizontal is denoted by θ, as shown in figure 1. We non–dimensionalize the Navier-Stokes equations using the height of the heavy fluid, $\bar{h}$, the buoyancy velocity, $\bar{u}_b$, and the initial concentration $\bar{C}_0$ and obtain

$$\nabla^2\psi = -\omega \tag{1}$$

$$\partial_t\omega + u_1\partial_{x_1}\omega + u_2\partial_{x_2}\omega = \frac{1}{Re}\nabla^2\omega - \partial_{x_1}(\cos\theta C) - \partial_{x_2}(\sin\theta C) \tag{2}$$

$$\partial_t C + \partial_{x_1}[(u_1 + U_s\sin\theta)C] + \partial_{x_2}[(u_2 - U_s\cos\theta)C] = \frac{1}{Pe}\nabla^2 C, \tag{3}$$

where $U_s = \bar{U}_s/\bar{u}_b$ and $Pe = \bar{u}_b\bar{h}/\kappa$ is the Péclet number, with κ the diffusion constant associated with $\bar{C}$. To facilitate numerical convergence [8], we set $Pe = Re$, or equivalently $\kappa = \nu$. The diffusion of C is not expected to be dynamically significant and this overestimate of κ only has a negligible impact.

Initially, the fluid is at rest, $\psi = \omega = 0$, and $C = 0$ everywhere except in a rectangle in the bottom left corner, $0 \le x_1 \le x_{fr}$, $0 \le x_2 \le 1$ where $C = 1$, see figure 1. The initial length of the current, x_{fr}, and the height of the computational domain, H, may be specified arbitrarily. We use a no–slip boundary condition at the top and bottom walls and a slip boundary condition at the left and right walls which allows the use of a Fourier transform of ψ along x_1.

$$\psi = \partial_{x_2}\psi = 0 \quad \text{at } x_2 = 0,\, H, \qquad\qquad \partial_{x_1x_1}\psi = \psi = 0 \quad \text{at } x_1 = 0,\, L,$$

where L is the length of the computational domain.

The concentration flux at the boundary, F, is set to 0 at the top and left walls

$$F = CU_s\cos\theta + \frac{1}{Pe}\partial_{x_2}C = 0 \quad \text{at } x_2 = H \tag{4}$$

$$F = -CU_s\sin\theta + \frac{1}{Pe}\partial_{x_1}C = 0 \quad \text{at } x_1 = 0. \tag{5}$$

However, particles are allowed to deposit at the bottom and right walls so that $F = \hat{k}\cdot\hat{n}U_sC$ at $x_2 = 0$ and $x_1 = L$, with $\hat{k} = (-\sin\theta, \cos\theta)$ a vertical unit vector and $\hat{n}$ the unit outer normal at the boundary. The boundary conditions on C are therefore equivalent to setting the diffusive flux to 0:

$$\partial_{x_2}C = 0 \quad \text{at } x_2 = 0, \qquad \partial_{x_1}C = 0 \quad \text{at } x_1 = L. \tag{6}$$

The accumulation of particles at the bottom boundary may be found by integrating in time the particle flux out of suspension.

2.1 Energy balance

From the velocity and concentration fields, we compute an energy budget of the flow, in a manner similar to that of Necker *et al* [17]. Consistent with the

Boussinesq approximation, density variations influence the potential energy, E_p, but not the kinetic energy, K,

$$E_p = \int_V \vec{x} \cdot \hat{k} C dV, \qquad K = \int_V \frac{1}{2} \vec{u} \cdot \vec{u} dV$$

where V is the domain of the simulations and $\vec{x}$ the position vector so that the vertical height of a point is $y = \vec{x} \cdot \hat{k}$. The time–derivative of E_p satisfies

$$\begin{aligned} \frac{dE_p}{dt} &= \int_V \left[\frac{D\vec{x}}{Dt} \cdot \hat{k} C + y \frac{DC}{dt} \right] dV \\ &= \int_V \left[\vec{u} \cdot \hat{k} C + \nabla \cdot (y(U_s \hat{k} C + \frac{1}{Pe} \nabla C)) - (U_s C + \frac{1}{Pe} \hat{k} \cdot \nabla C) \right] dV \\ &= \int_V \vec{u} \cdot \hat{k} C dV + \oint_S y F dS - \int_V U_s C dV - \frac{1}{Pe} \oint_S C \hat{k} \cdot \hat{n} dS \end{aligned} \tag{7}$$

where S is the surface bounding V. Similarly, the time–derivative of the kinetic energy is (see Batchelor [18]).

$$\begin{aligned} \frac{dK}{dt} &= \int_V \frac{1}{2} \frac{D\vec{u} \cdot \vec{u}}{Dt} dV = \int_V \left[-\nabla \cdot (P\vec{u}) + \frac{1}{Re} \vec{u} \cdot \nabla^2 \vec{u} - \vec{u} \cdot \hat{k} C \right] dV \\ &= - \int_V \frac{2}{Re} \bar{\bar{s}} : \bar{\bar{s}} dV - \int_V \vec{u} \cdot \hat{k} C dV \end{aligned} \tag{8}$$

where $\bar{\bar{s}} = (1/2)(\nabla \vec{u} + (\nabla \vec{u})^T)$. Therefore, the total energy present in the system is

$$\begin{aligned} E_p + K\Big|_{t=0} &= E_p + K + \\ &\int_0^t \Big[- \oint_S y F dS + \frac{1}{Pe} \oint_S C \hat{k} \cdot \hat{n} dS + \int_V \left(U_s C + \frac{2}{Re} \bar{\bar{s}} : \bar{\bar{s}} \right) dV \Big] dt \\ &\qquad \text{(I)} \qquad\qquad \text{(II)} \qquad\qquad \text{(III)} \quad \text{(IV)}. \end{aligned} \tag{9}$$

The term (I) accounts for the loss of potential energy through particle deposition; (II) indicates the variation in potential energy due to diffusion of C and is typically negative as larger concentrations diffuse upward; (III) reflects the loss of potential energy as particles in suspension travel downward, and (IV) measures viscous dissipation.

3 Numerical approach

In order to simulate turbidity currents over a broad range of situations, we allow the angle between the horizontal and the bottom surface, θ, to depend on

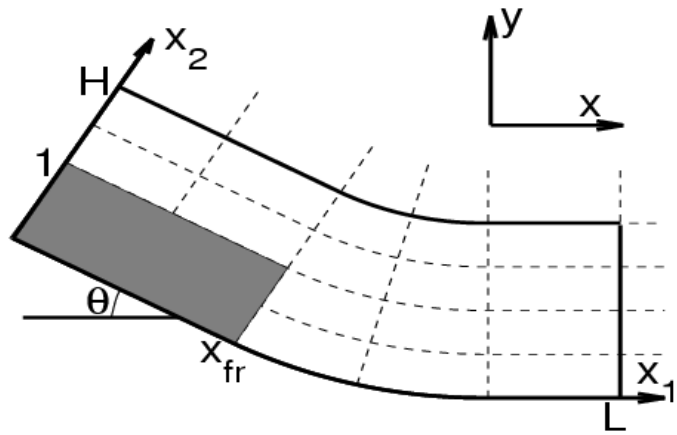

Fig. 1. Schematic of the coordinate system used in the simulations. The angle θ between the x_1-axis and the horizontal is allowed to vary with x_1 to model varying slopes. The dark region corresponds to the initial position of heavy fluid and is constrained by $0 \leq x_1 \leq x_{fr}$, $0 \leq x_2 \leq 1$. The height and length of the computational domain are H and L, respectively.

x_1. Our coordinate system (x_1, x_2), illustrated in figure 1, is therefore related to Cartesian coordinates, x in the horizontal and y in the vertical, through

$$x = \int_0^{x_1} \cos\theta(x_1')dx_1' + x_2 \sin\theta(x_1) \tag{10}$$

$$y = -\int_0^{x_1} \sin\theta(x_1')dx_1' + x_2 \cos\theta(x_1). \tag{11}$$

Effectively, we thus consider a spatially varying gravity vector and use a rectangular computational domain. For the sake of simplicity, we have neglected corrections to equations (1)-(3) resulting from the curvilinear nature of this coordinate system. These corrections are of order $x_2 d\theta/dx_1$ and we therefore restrict our study to systems where $\xi = Hd\theta/dx_1 \ll 1$ to ensure that the neglected terms are everywhere small. Note that here ξ represents the ratio of the height of the computational domain to the radius of curvature of the bottom surface; our simulations are expected to be valid only for relatively large curvature radii.

Our numerical method has several advantages. First, the use of highly resolved numerical simulations rather than layer averaged equations allows for direct measurements of quantities such as the bottom stress, dissipation and front velocity. Moreover, using a streamfunction–vorticity formulation satisfies the continuity equation exactly and does not require any approximation of the pressure field. In contrast, previous simulations aimed at modeling gravity currents have either assumed a hydrostatic pressure directly [19] or through layer averaged equations [13], [20]. Third, the use of a varying gravitational vector in a rectangular computational domain allows for a simple, flexible and efficient implementation of the governing equations and boundary conditions

for any bottom surface, provided $\xi \ll 1$. In particular, spectral methods may be used, thereby improving the accuracy of the simulations at little computational cost. Although an exact mapping between the physical and computational domains is possible, its implementation is comparatively cumbersome and computationally extensive [21]. We investigate the importance of the neglected curvature terms by tracking conserved quantities such as mass and energy in §4.

The numerical integration of equations (1)-(3) is performed in a manner similar to that of Härtel, Meiburg & Necker [8]. We use sixth order compact finite differences for C everywhere and for ψ along x_2 and a Fourier transform for ψ in the x_1-direction; near the boundaries the derivatives are accurate to third order [22]. A third order Runge-Kutta integrator is used to march equations (2)-(3) forward in time [8]. Equation (1) is then solved by taking a Fourier transform of the vorticity in the x_1-direction and using 5-point compact finite differences in x_2 [22]. The velocity field is obtained by differentiating ψ. We use an adaptive time-step to satisfy the CFL and diffusive stability criteria while minimizing computation time.

4 Numerical results

A sample of the concentration (at thre different times) and vorticity fields obtained via our numerical simulations is shown in figures 2a-c and 2d, respectively. Here the current is initially propagating down a 5° slope, figure 2a at $t = 2$, before reaching a horizontal region, figure 2b at $t = 14$ and eventually losing its structure, figure 2c at $t = 30$. At early times, we observe a well defined current, with a head significantly higher than the trailing fluid. Vortices are being shed above and behind the head, mostly rotating counterclockwise. These vortices are seen to entrain ambient fluid and their concentration is reduced relative to that of the main current. The head of the current is here slightly overhanging, trapping a region of clear fluid below heavy fluid, a typical feature of gravity currents traveling down an incline, [10], [11]. The vorticity is greatest in the vortices shed above the head and near the bottom, no–slip wall. Clockwise vortices of lesser intensity are also seen to form within the current.

4.1 Convergence

We first verify the numerical convergence of our simulations by tracking the total energy of the system, using equation 9, while varying the grid size. We fix the geometry of the domain to $\theta = 10°$ for $x_1 \leq 7$, $\theta = 0°$ for $9 \leq x_1$,

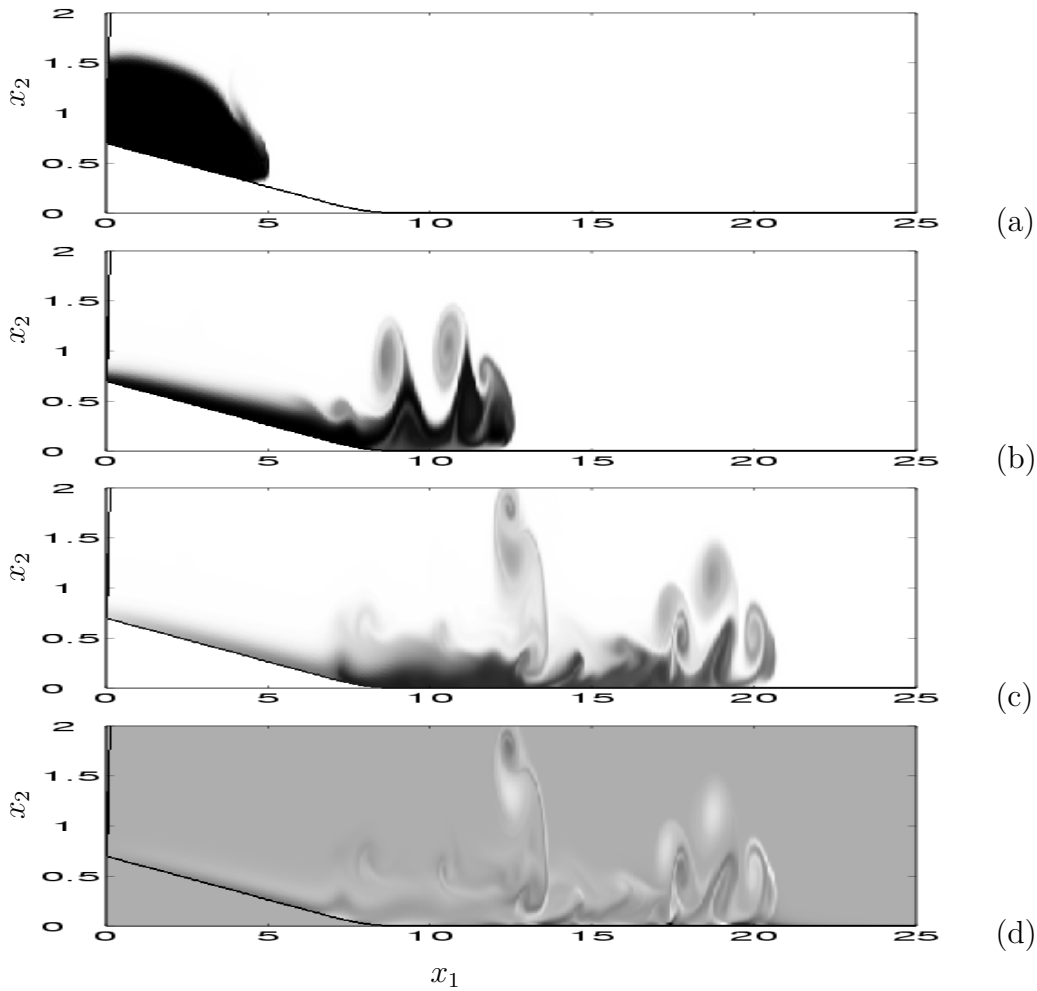

Fig. 2. Concentration field of a density–driven gravity current at $t = 2$, (a), $t = 14$ (b) and $t = 30$ (c). The dark regions correspond to high solute concentration. d) Vorticity field of the same current, the dark regions correspond to negative (clockwise) vorticity and the pale regions to positive vorticity. The current displayed here traveled down a complex geometry: $\theta = 5^\circ$ for $x_1 \leq 7$, $\theta = 0^\circ$ for $x_1 \geq 9$ and θ varying linearly in the intermediate region. Other governing parameters are $Re = Pe = 2,200$, $H = 3$, $L = 32$ and $x_{fr} = 4$

and θ linearly varying in the intermediate region. We set $H = 1$ and $L = 32$ and denote by n_{x_1} and n_{x_2} the number of points along the x_1 and x_2-axis, respectively.

Numerical instabilities are generated near the front of the current and along the most vigorous vortices when relatively coarse grids are used ($n_{x_1} \leq 257$, $n_{x_2} \leq 33$ for $Re = Pe = 2,200$). However, increasing slightly the resolution ensures that the flow remains numerically stable. The number of grid points required to avoid the formation of instabilities is seen to increase with Re, but as a general rule, instabilities may be avoided provided the smaller structures of the flow, which scale as $Re^{-1/2}$, can be resolved.

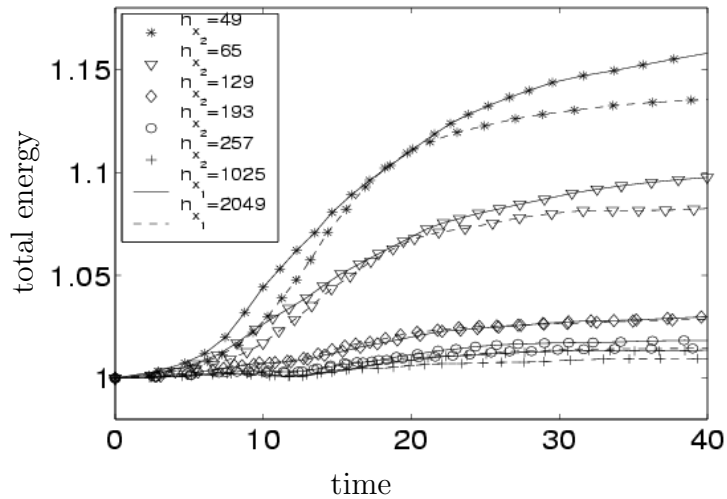

Fig. 3. Time dependence of the total energy present in the system for different grid sizes. The initial energy is normalized to 1. The number of points in the streamwise and perpendicular directions are denoted by n_{x_1} and n_{x_2}, respectively. The geometry modeled here is that of a varying slope: $\theta = 10^\circ$ for $0 \leq x_1 \leq 7$, $\theta = 0^\circ$ for $9 \leq x_1 \leq 32$, and θ decreasing linearly in the intermediate region. These computations simulate density–driven currents ($U_s = 0$) and were performed with $Pe = Re = 2,200$, $H = 1$, $L = 32$ and $x_{fr} = 4$.

Figure 3 shows the total energy as a function of time for various mesh sizes. It may be seen that doubling n_{x_1} provides only slightly better energy conservation. In contrast, the number of points along the x_2-axis (n_{x_2}) is determinant in avoiding the generation of an energy surplus. As the grid is refined, the error progressively drops below 1%, even after 40 time units when the current has lost most of its structure. For $n_{x_1} \geq 1025$ and $n_{x_2} \geq 193$, the error on the total energy improves only slightly with further mesh refinement. The qualitative features of the current also remain virtually unchanged: vortices appear well resolved and the structure and velocity of the current are independent of mesh size.

4.2 Influence of the radius of curvature

We now investigate the influence of $\xi = Hd\theta/dx_1$ on the conservation of the total mass of the heavy fluid present in our simulations. In order to focus on the impact of the corner geometry, we vary only the transition length, i.e. the length over which the bottom slope decreases from $\theta = 10^\circ$ to $\theta = 0^\circ$. Figure 4 shows the time evolution of the total mass of heavy fluid present in the computational domain for different values of ξ. At early times, $t < 3.9$, the current overlies a region of constant slope angle and the mass is conserved nearly exactly. As the current reaches the corner region, mass is effectively lost due to the neglect of curvature terms. As the transition from sloping

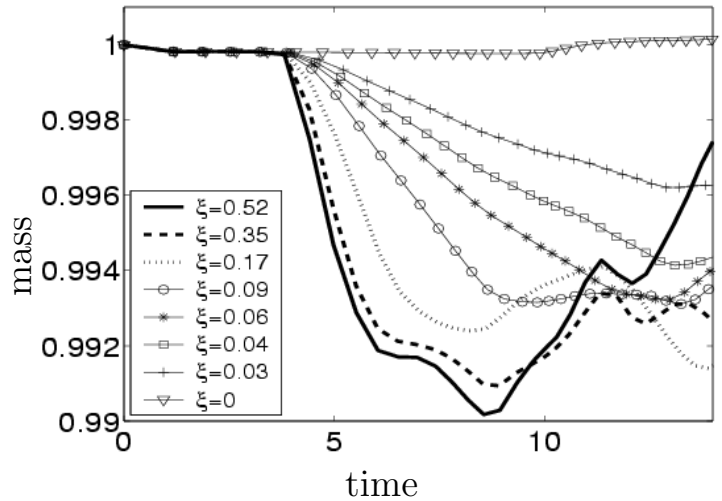

Fig. 4. Time dependence of the total mass of heavy fluid for corners of various sharpness. The ratio of the height of the domain to the curvature radius is denoted by $\xi = Hd\theta/dx_1$. For all cases shown, the initial and final angles are 10° and 0°, respectively, except for $\xi = 0$ where the slope angle is constant at $\theta = 10°$. These computations simulate density–driven currents ($U_s = 0$) and were performed with $Pe = Re = 2,200$, $H = 1$, $L = 16$ and $x_{fr} = 4$.

to horizontal bottom occurs more abruptly (larger ξ), larger mass losses are observed. Because mass losses are mostly restricted to the region overlying the bottom corner, the local error, which may be approximated as the total error divided by the transition length, increases even more abruptly with ξ. However, the total mass of the system remains greater than 99% of its initial value due to the opposing effects of increased curvature and reduced transition length.

For transition lengths comparable to the initial length of the heavy fluid, x_{fr}, the local error, taken to be the total mass loss divided by the approximate mass of fluid in the corner, is estimated to remain of the order of a few percent, e.g. 3% for $\xi = 0.09$ and 1% for $\xi = 0.04$. Once the head has reached the horizontal region, the total mass of heavy fluid fluctuates between its initial value and the minimum observed in figure 4, as vortices cross over to the horizontal region. At later times, the quantity of heavy fluid overlying the curved region decreases and the total mass returns to a value close to the initial mass.

4.3 Front velocity

Figure 5 shows the time–dependence of the front velocity of currents traveling over a horizontal surface, a constant slope angle $\theta = 10°$ and a varying slope where $\theta = 10°$ for $x_1 \leq 3.5$ and $\theta = 0°$ for $x_1 \geq 5.5$. After a brief acceleration period, currents traveling over a bottom surface of constant angle ($\theta = 0°$ or $\theta = 10°$) quickly achieve a constant velocity. As expected, currents traveling

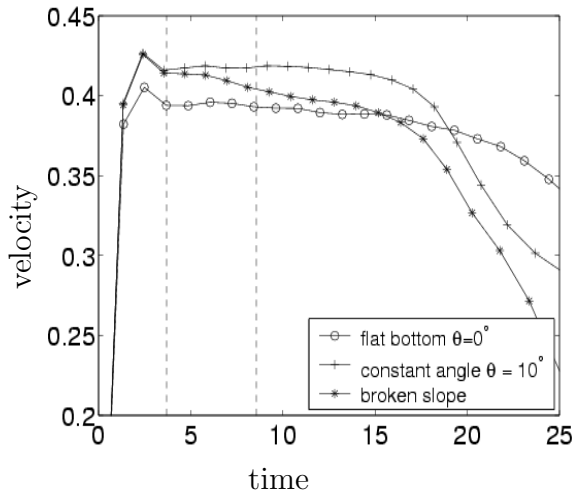

Fig. 5. Time dependence of the velocity of gravity currents propagating over a horizontal surface (o), varying slope with initial angle $\theta = 10^\circ$ and $\xi = 0.06$ ($*$) and constant slope angle $\theta = 10^\circ$ ($+$). The dashed lines indicate the time when the varying slope current overlies the curved bottom. These computations simulate density-driven currents and were performed with $Re = Pe = 2,200$, $H = 1$, $L = 16$ and $x_{fr} = 2$.

down an inclined slope propagate faster than those spreading on a horizontal surface. The velocity of the current propagating along a varying slope is initially equal to that of a current traveling down a 10° slope. As the current reaches the corner, shown as the first dashed line in figure 5, its velocity is reduced. By the time the head of the current overlies a horizontal surface, second dashed line, its velocity approaches that of a current traveling along a horizontal bottom. However, the velocity of the current traveling down a varying slope remains slightly larger than its horizontal counterpart. The inertia of the current thus affects its velocity over a significant time period and both the final and initial slope angles must be considered to determine the instantaneous velocity of the current.

At longer times, the velocity of all currents decreases as the height of the head is reduced. When observing animations of our simulations, a bore caused by the reflection of the light fluid on the left wall is seen to propagate downstream. Similar bores have been observed experimentally by Bonnecaze, Huppert & Lister [7] and were seen to travel faster than the head of the current. Although the presence of large vortices in the wake of the current renders the systematic tracking of the bore difficult, it is usually seen to overtake the head (at $t = t_o$). This significantly reduces the height of the front of the current, which in turn causes the front velocity to decrease. Along an inclined bottom, the bore catches up with the head earlier, $t_o = 17$, than along a horizontal surface, $t_o = 25$, allowing the horizontal current to travel faster than its inclined counterpart for $t > 18$. For the varying slope current, the bore velocity appears to be almost unchanged as the current reaches the horizontal region. The bore therefore also

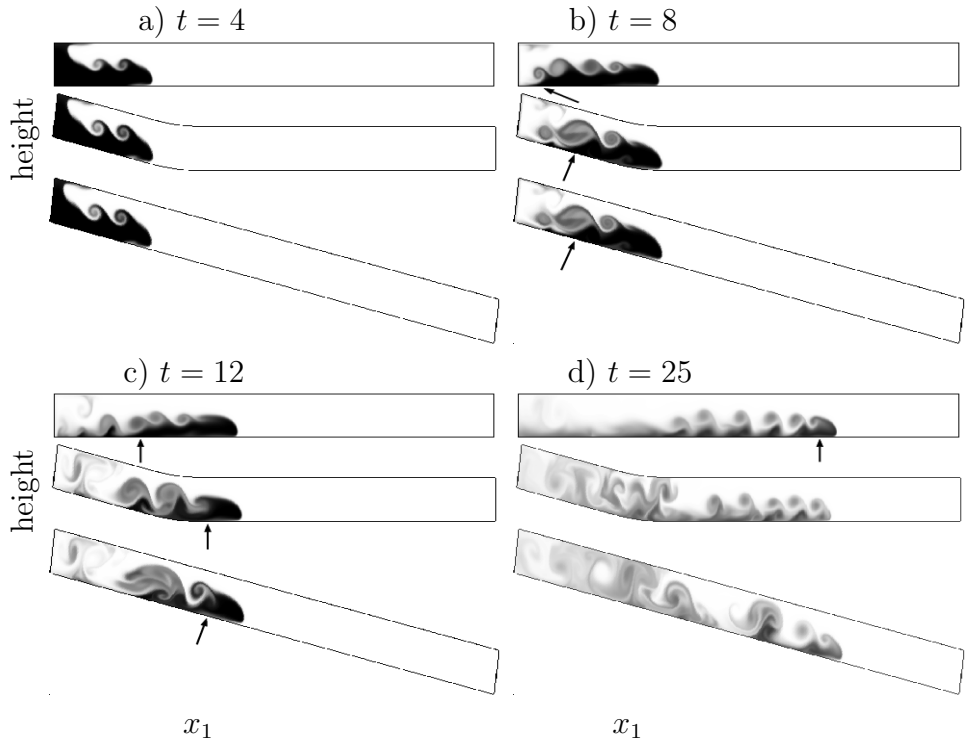

Fig. 6. Snapshots of the evolution of the concentration of heavy fluid propagating along a horizontal surface (above), varying slope with initial angle $\theta = 10^\circ$ (center) and constant slope $\theta = 10^\circ$ (bottom). The dark regions correspond to high concentrations of heavy fluid. The boundary of the computational domain is outlined in black. Pictures are taken at: a) $t = 4$, before the varying slope current reaches the corner, b) $t = 8$, as it reaches the horizontal region, c) $t = 12$, shortly afterward and d) $t = 25$, when the currents have lost most of their structure. The arrows indicate the approximate location of the bore. The simulations shown here were performed with $Re = Pe = 2,200$, $H = 1$, $L = 16$ and $x_{fr} = 2$.

overtakes the head near $t = 17$, well before it overtakes the horizontal current.

It should be noted that such bores only overtake the head for certain initial lengths of the heavy fluid, i.e. $1 \leq x_{fr} \leq 3$. For other values of x_{fr}, the vortices shed behind the head appear to disperse the bore before it has time to reach the head of the current. Also, if the height of the computational domain is increased to $H \geq 2$, the backflow of light fluid is weaker and no bores are observed.

Figure 6 compares the progression of gravity currents in three different geometries: horizontal surface, varying and constant slope. As is to be expected, the current traveling down a varying slope initially resembles that traveling down a constant slope (figure a). In particular, the vortices shed behind the head are more vigorous than for currents propagating over a horizontal surface, thereby increasing the amount of mixing between light and heavy fluid. However, as it reaches the horizontal region, the varying slope current is progressively mod-

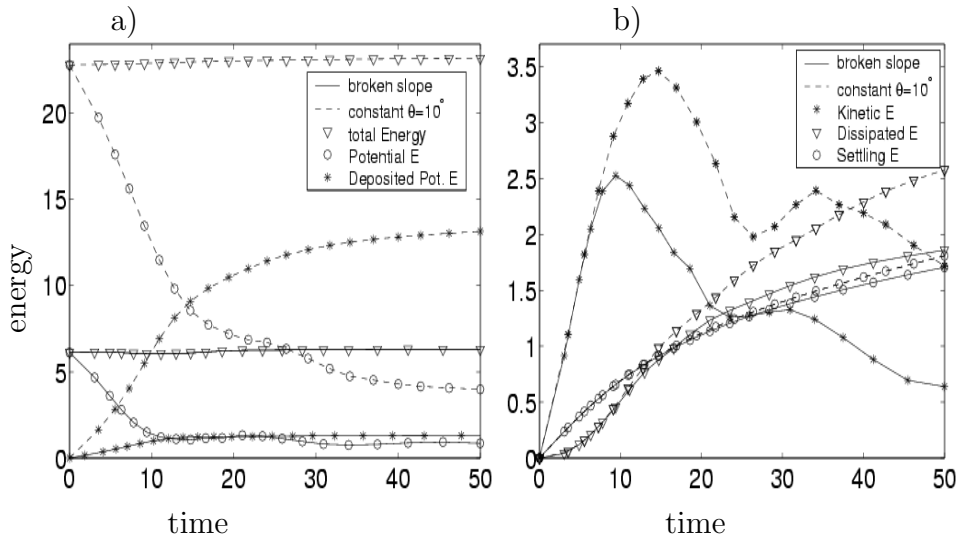

Fig. 7. Time–dependence of the energy distribution of particle–driven currents traveling down a constant slope $\theta = 10°$ (dotted line) and a varying slope (solid line). a) Total energy ($\triangledown$), potential energy (o), and potential energy of deposited particles ($*$). Note that here the height of level 0 is taken to be the lowest point of the computational domain. b) Kinetic energy ($*$), dissipated energy (o) and energy lost owing to particle settling ($\triangledown$). All the energy terms are computed according to equation 9. The computations shown here were performed with $Re = Pe = 2,200$, $U_s = 0.02$, $H = 3$ and $x_{fr} = 4$.

ified and begins to resemble a horizontal current. Smaller vortices are shed behind the head and the velocity is reduced, in agreement with the behavior of horizontal currents, (figures b-c). At long times, it may be seen that vigorous mixing has occurred in the inclined regions; however, very little heavy fluid has been transported into the upper half of the computational domain in regions overlying a horizontal surface (figure d). The bore caused by the reflection of the light fluid, indicated with black arrows, may be seen to trail the head of the inclined and varying slope currents in figure c and has already overtaken the head at $t = 25$ (figure d).

4.4 Energy distribution

Figure 7 shows the different terms of the energy budget (equation 9) of particle–driven currents traveling down a constant or varying slope. In figure 7a, the potential energy, shown as (o) is calculated relative to the lowest point of the computational domain, thus giving an initial energy three times larger to the current traveling down a constant slope than to that on a broke slope. Particles reaching the bottom boundary retain their potential energy, ($*$), which therefore is no longer available to the gravity current. A large fraction of the total initial energy is lost through this mechanism, particularly for

constant slope currents, rendering the conversion of potential to kinetic energy rather inefficient. In the horizontal section of the varying slope current, deposited particles have zero potential energy.

In figure 7b, we plot the kinetic, dissipated and settling energy for the same two currents. Initially, the varying slope current travels over an inclined region and the energy distribution is the same for both currents. As the varying slope current reaches the horizontal region, its velocity is reduced and its kinetic energy is seen to become significantly smaller than that of the inclined current. Similarly, the dissipated energy of the varying slope current increases more slowly once the current overlies the horizontal region, the vortices shed behind the head being weaker in that region. However, the potential energy lost through particle settling is virtually unaffected by the geometry, as particles travel approximately the same distance relative to the fluid. The energy gained by the system through the action of particle diffusion is not shown here as it remained less than 1.2% of the total energy throughout the simulations.

5 Discussion

We have performed two–dimensional numerical simulations of gravity currents propagating over slopes of varying angle. Our computations were seen to be consistent with numerical results obtained by previous authors in simpler geometries [8], [9]. The main qualitative features of the flow observed in our simulations also agree well with experimental descriptions of gravity currents, such as the formation of a bore [7], the speed variation of the nose of the current as it reaches the horizontal region and the entrainment of ambient fluid by currents traveling over an inclined bottom [11]. Provided the radius of curvature of the bottom surface is much larger than the height of the computational domain, i.e. $\xi = Hd\theta/dx_1 \ll 1$, our approach allows the simulation of an arbitrary bottom geometry. Despite neglecting the curvature terms, our simulations were seen to conserve mass within 1% and energy within 5% for $\xi \leq 0.09$. Complex three–dimensional geometries may also be modeled through the use of a spatially varying gravity vector and will be the subject of future research. In particular, currents traveling through channels may be simulated using a three-dimensional extension of the approach presented here.

To the best of our knowledge, the influence of particle resuspension in turbidity currents has not yet been investigated via highly resolved numerical simulations. Our model may easily be extended to include a non–zero particle flux at the bottom boundary, and future research will focus on characterizing the influence of particle reentrainment on the dynamics of gravity currents. We anticipate from observations of the bottom shear stress that the angle of inclination will be a dominant factor in determining whether a current is

predominantly eroding or depositing. Direct numerical simulations of particle resuspension in complex three–dimensional geometries should allow for a more complete and realistic description of gravity currents and their deposits.

The advantage of high resolution numerical simulations over layer averaged models lies in the absence of empirical relations characterizing the effects of dissipation, turbulence or fluid entrainment. Precise estimates of quantities such as the bottom shear stress, fluid entrainment and turbulent dissipation may be computed directly from our simulations. However, numerical stability considerations render exceedingly slow the simulation of very high Reynolds number currents ($Re \sim 10^7$) such as those appropriate in geophysical contexts. A possible avenue for future research would be to combine these two approaches, using high resolution numerical simulations for $Re \sim 2,000$ to determine the coefficients needed in layer–averaged simulations or turbulence models. Such simplified models may then be used to simulate high Reynolds number flows.

Acknowledgments

The authors wish to thank Vineet Birman for his help in writing up the code. We also thank Ben Kneller and Mosche Strauss for helpful discussions. We also acknowledge the financial support of BHP and the National Science Foundation.

References

[1] J. Simpson, Gravity currents in the environment and the laboratory, Cambridge University Press, 1987.

[2] R. Sparks, S. Carey, H. Sigurdsson, Sedimentation from gravity currents generated by turbulent plumes, Sedimentology 38 (1991) 839–856.

[3] G. Parker, M. García, Y. Fukushima, W. Yu, Experiments on turbidity currents over an erodible bed, J. Hydr. Res. 25 (1987) 191–244.

[4] B. Kneller, Beyond the turbidite paradigm: physical models for deposition of turbidites and their implications for reservoir prediction., In Hartley & Prosser, Characterisation of Deep Marine Clastic Systems Geological Society of London Special Publication, 94, 29–46 (1995).

[5] J. Bush, B. Thurber, F. Blanchette, Particle clouds in homogeneous and stratified environments, J. Fluid Mech. 489 (2003) 29–54.

[6] M. García, G. Parker, Entrainment of bed sediment into suspension, J. Hydr. Eng. 117 (1991) 414–435.

[7] R. Bonnecaze, H. Huppert, J. Lister, Particle–driven gravity currents, J. Fluid Mech. 250 (1993) 339–369.

[8] C. Härtel, E. Meiburg, F. Necker, Analysis and direct numerical simulation of the flow at a gravity current head. part 1. flow topology and front speed for slip and no–slip boundaries, J. Fluid Mech. 418 (2000) 189–212.

[9] F. Necker, C. Härtel, L. Kleiser, E. Meiburg, High–resolution simulations of particle–driven gravity currents., Int. J. of Multiphase Flow 28 (2002) 279–300.

[10] R. Britter, P. Linden, The motion of the front of a gravity current traveling down an incline, J. Fluid Mech. 99 (1980) 531–543.

[11] P. Beghin, E. Hopfinger, R. Britter, Gravitational convection from instantaneous sources on inclined boundaries, J. Fluid Mech, 107 (1981) 407–422.

[12] M. García, G. Parker, Experiments on the entrainment of sediment into suspension by a dense bottom current, J. Geo. Res. 98 (1993) 4793–4807.

[13] M. García, Depositional turbidity currents laden with poorly sorted sediment, J. Hydr. Engr.

[14] A. Bouma, W. Normark, N. Barnes, Submarine fans and related turbidite systems, Frontiers in sedimentary geology, Springer-Verlag, 1985.

[15] I. Wood, J. Simpson, Jumps in layered miscible fluids, J. Fluid Mech 140 (1984) 329–342.

[16] Y. Kubo, T. Nakajima, Laboratory experiments and numerical simulation of sediment-wave formation by turbidity currents, Mar. Geol. 192 (2002) 105–121.

[17] F. Necker, C. H. anf L. Kleiser, E. Meiburg, Mixing and dissipation in particle-driven gravity currents, J. Fluid Mech., to appear.

[18] G. Batchelor, An introduction to fluid dynamics, Cambridge mathematical library, 1972.

[19] M. Felix, A two–dimensional numerical model for a turbidity current, Spec. Publs. int. Ass. Sediment. 31 (2001) 71–81.

[20] P. Montgomery, T. Moodie, Two-layer gravity currents with topography, Stud. Appl. Math. 102 (1999) 221–266.

[21] K. Winters, H. Seim, T. Finnigan, Simulation of non-hydrostatic, density-stratified flow in irregular domains, Int. J. Num. Met. Fluids 32 (2000) 263–284.

[22] S. Lele, Compact finite difference schemes with spectral–like resolution, J. Comp. Phys. 103 (1992) 16–42.